

Vertex Simulation of Grain Growth in the Presence of Zener Pinning Effect

N. MAAZI*

Laboratoire Microstructures et Défauts dans les Matériaux (LMDM), Département de Physique, Faculté des Sciences Exactes, Université Mentouri Constantine1, 25000 Constantine, Algeria

Received: 30.11.2022 & Accepted: 06.02.2023

Doi: [10.12693/APhysPolA.143.336](https://doi.org/10.12693/APhysPolA.143.336)

*e-mail: nmaazi@yahoo.fr

In this study, we investigated the pinning effect exerted by second-phase particles on grain growth. To overcome the difficulties, mainly linked to the complex topological events while using the standard vertex technique in the presence of particles, a modified version of grain growth simulation is presented. The simulation is based on input data from electron backscatter diffraction measurements. Two hexagonal lattices discretize the physical space. One grid stores the grain orientation data, i.e., Euler's angles ($\varphi_1, \varphi, \varphi_2$). Nodes (vertices) are located in the second grid, where particles are randomly distributed. Vertex simulations, by mean triple junctions dynamics only, were performed to highlight the influence of the surface fraction of the particles on the grain size distribution, the limiting mean grain size, and the edges per grain distribution. During the simulation procedure, vertices move in the direction of the effective force, which results from the driving and the pinning forces.

topics: EBSD, grain growth, vertex simulation, particles pinning

1. Introduction

The physical and mechanical properties of polycrystalline materials, such as metallic alloys and ceramic composites, are greatly controlled by their microstructures. Grain growth has been the subject of active research over the past decades, due to its importance in controlling the microstructures of final materials [1]. Normal grain growth is a process through which the average grain size \bar{R} increases in time as a result of the vanishing of small grains. The presence of second-phase particles in polycrystals plays an important role in inhibiting normal grain growth during thermal treatment by pinning their grain boundaries (GBs) [2]. The interaction of particles with GBs, which is referred to as "Zener pinning" [3], is of high technological importance in the manufacture of materials, such as magnetic alloys Fe-3%Si [4]. To investigate the influence of particles on the grain growth process, a variety of computational methods have been used, such as Monte Carlo (MC) Potts [5, 6], vertex or front-tracking [7, 8], molecular dynamics [9, 10], cellular automata [11, 12], and phase field [13, 14]. Of these numerical techniques, the MC Potts method has been largely used in the simulation of polycrystals at a mesoscopic scale. The extensive use of this technique results from its computational simplicity. However, the significant drawback of this approach

is the relation between the Monte Carlo time and the physical time. In the phase field method, field variables are employed as parameters to represent the microstructure. Although this method is widely used, its enormous computational cost has been the main drawback of multi-orientation field variables [15]. The vertex method presents a physical way to simulate the grain growth phenomena. Unfortunately, although this method is potentially the best one to explore normal grain growth, it is hardly used due to the difficulties, mainly linked to detecting and solving the system topology, which evolves continuously during grain growth. In spite of these difficulties, this technique has been used in other natural structures, e.g., for the growth of ice in glaciology [16] and cells in biology [17]. The complex topological events, e.g., the shrinkage of grains and the influence of neighborhood on individual grains, are difficult to manage during the simulation procedure. To avoid these problems, modifications to the vertex model have been suggested in a recent work [18]. This technique usually begins with using a matrix generated by Voronoi tessellation [19, 20]. In the present work, an experimental microstructure obtained from electron backscatter diffraction (EBSD) measurements, where the grain area is discretized, is used as input data. The microstructure is represented on a fixed hexagonal lattice (microstructure grid), which stores the grain

orientation data. Neighboring points with the same and different orientations define grains and GBs, respectively. In the presence of second-phase particles, serious difficulties were encountered while using the standard vertex technique, e.g., complex topological changes due to vertices–particles interactions. To surmount these obstacles, one suggested that triple and double junctions (vertices) are from a second lattice (vertices grid) where particles are randomly distributed. However, no orientation is distributed to particles. The individual effective force, which is the force resulting from the driving and the pinning forces, is easily calculated. This force is directly introduced into the vertex motion equation. Therefore, vertices move toward its direction. These modifications improve the vertex simulation efficiency.

2. Modification of the vertex method in the presence of particles

In the vertex models [21, 22], the triple junctions (real vertices) were supposed to govern the whole-grain growth process. The evolution of the microstructure is described by the displacement of these nodes (vertices), which is accurately described from a physical viewpoint. The resultant of grain boundary tensions is considered the only driving force acting upon triple junctions. So, the vertex moves in its direction with the speed

$$\mathbf{v}_i = m_i \sum_{j=1}^3 \gamma_{ij} \frac{\mathbf{r}_{ij}}{|\mathbf{r}_{ij}|}, \quad (1)$$

where m_i is the mobility of the vertex i , γ_{ij} is the energy per unit length of grain boundary between real vertices i and j , and \mathbf{r}_{ij} is the vector connections vertex i to vertex j .

In the presence of immobile particles, Tamaki et al. [23] have studied the interaction between particles and GBs, in a two-dimensional vertex model, by considering the grain boundary energy minimum as the evaluation function. However, the complex topological changes due to vertices–particles interactions are difficult to manage and can be a very complex task. In another work, Weygand et al. [7] introduced the pinning effect of particles in the vertex model through a critical angle φ_{cr} . During the grain growth simulation, vertices are pinned when they intersect particles (active particles) and will be unpinned as soon as φ becomes greater than φ_{cr} (Fig. 1a),

$$\sin(\varphi_{cr}) = \frac{F_{cr}}{2\gamma}, \quad (2)$$

where F_{cr} is the pinning force, and γ is the grain boundary energy.

As shown in Fig. 1a, (2) is true only for the case of virtual vertices (double junctions) where the driving force F_d is given by

$$F_d = 2\gamma \sin(\varphi). \quad (3)$$

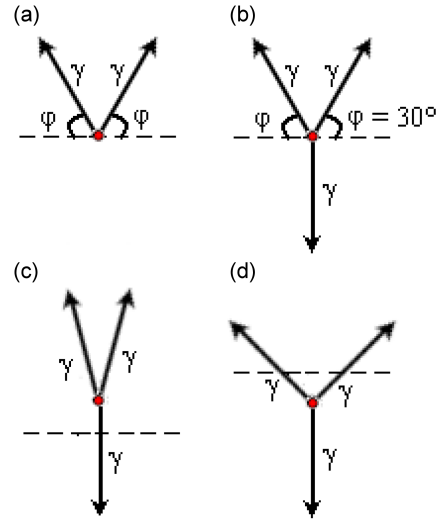


Fig. 1. Driving force for: double junctions (a), and triple junctions $\varphi = 30^\circ$ (b), $\varphi > 30^\circ$ (c), and $\varphi < 30^\circ$ (d).

For triple junctions, (2) is not valid. The driving force F_d will be (Fig. 1b, c, and d)

$$F_d = \gamma |2 \sin(\varphi) - 1|. \quad (4)$$

One can distinguish three cases:

1. the vertex does not move (triple point equilibrium) if $2 \sin(\varphi) = 1$, i.e., $\varphi = 30^\circ$ (Fig. 1b);
2. the vertex moves up if $2 \sin(\varphi) > 1$, i.e., $\varphi > 30^\circ$ (Fig. 1c);
3. the vertex moves down if $2 \sin(\varphi) < 1$, i.e., $\varphi < 30^\circ$ (Fig. 1d).

The motion of triple junctions affects the motion of the boundaries. Many works focus on the influence of triple junctions on grain growth [10, 24–27]. It has been demonstrated that the motion of triple junctions can have a significant effect on the resulting grain growth. In a recent work [18], the global features of the grain growth process were best reproduced by using triple junction motion. However, one considers only triple junction dynamics in the present work. The effect of a particle is explained by considering the pinning force \mathbf{F}_f , which counteracts the driving force. In 2D, the maximum pinning force is given by [28]

$$F_f = 2\gamma. \quad (5)$$

The pinning force can be incorporated directly into (1). So, the triple junctions speed becomes

$$\mathbf{v}_i = m_i \left(\sum_{j=1}^3 \gamma_{ij} \frac{\mathbf{r}_{ij}}{|\mathbf{r}_{ij}|} - \mathbf{F}_f \right). \quad (6)$$

Instead of using the critical angle φ_{cr} to simulate grain growth, the influence of particles on grain growth can be incorporated into the simulation procedure through (6). However, no topological assumptions are made about the complex GBs–particles interactions. During the simulation procedure, in each

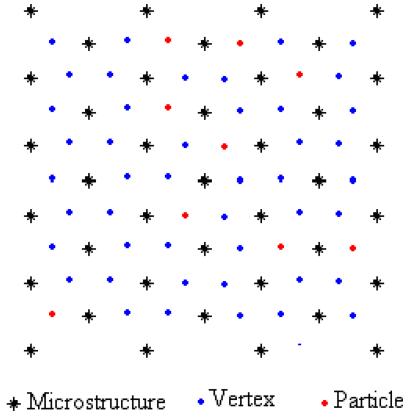


Fig. 2. Microstructure and vertices lattices used in the simulation.

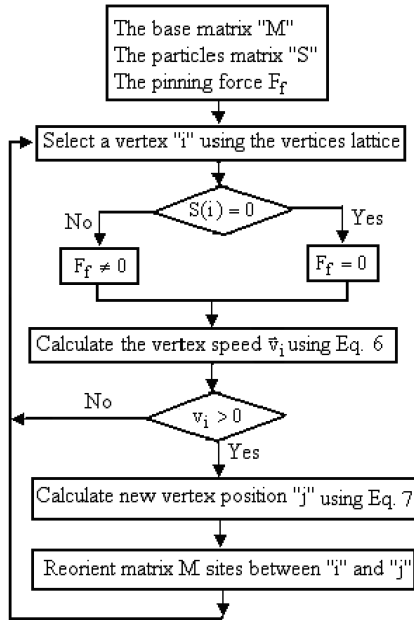


Fig. 3. Simulation algorithm proposed for grain growth in the presence of particles.

time increment Δt , the new positions of the vertices are calculated using the following relation

$$\mathbf{r}_i(t + \Delta t) = \mathbf{r}_i(t) + \mathbf{v}_i(t) \Delta t, \quad (7)$$

where the velocity vector $\mathbf{v}_i(t)$ is obtained from (6).

The flexibility of vertex dynamics is a powerful tool to investigate the effect of second-phase particles on grain structure evolution, but the price to pay is the difficulty of managing the topological changes. To avoid these obstacles, the simulation is done simultaneously with two hexagonal lattices. One lattice stores the matrix grains orientation data (M), where the orientation of each site is defined by three Euler's angles $(\varphi_1, \varphi, \varphi_2)$. So, the microstructure is easily reconstituted. Vertices are located in the second lattice (Fig. 2). It is important to note

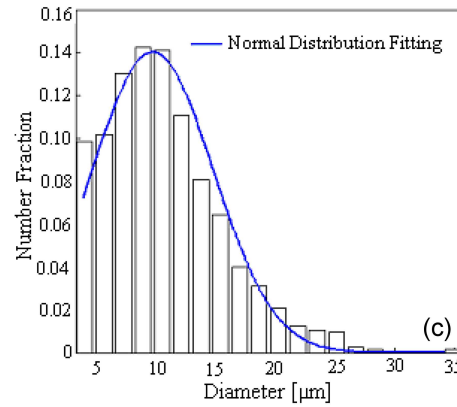
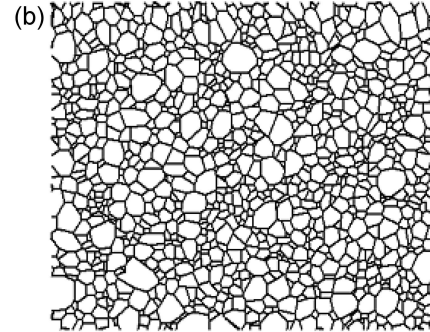
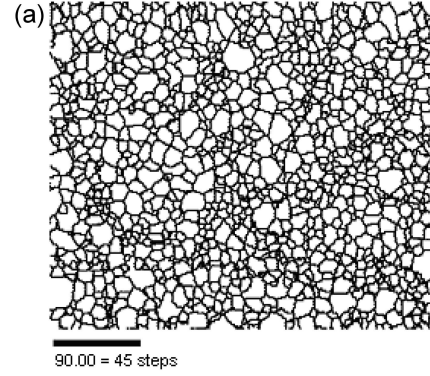


Fig. 4. Initial microstructure measured by EBSD (a), the corresponding straight boundaries (b), and the size distribution (c).

that all vertices are real. Therefore virtual vertices do not exist. The present simulation procedure is shown in Fig. 3.

The particles matrix "S" is defined as follows

$$S(i) = \begin{cases} 1 & \text{active particle at vertex } (i), \\ 0 & \text{no particle at vertex } (i). \end{cases} \quad (8)$$

The size of "S" is equal to the vertices lattice size.

3. Conditions of the simulation

The simulation begins by using an experimental microstructure Fe-3%Si obtained from electron backscatter diffraction (EBSD) measurements (Fig. 4a). This microstructure is constituted

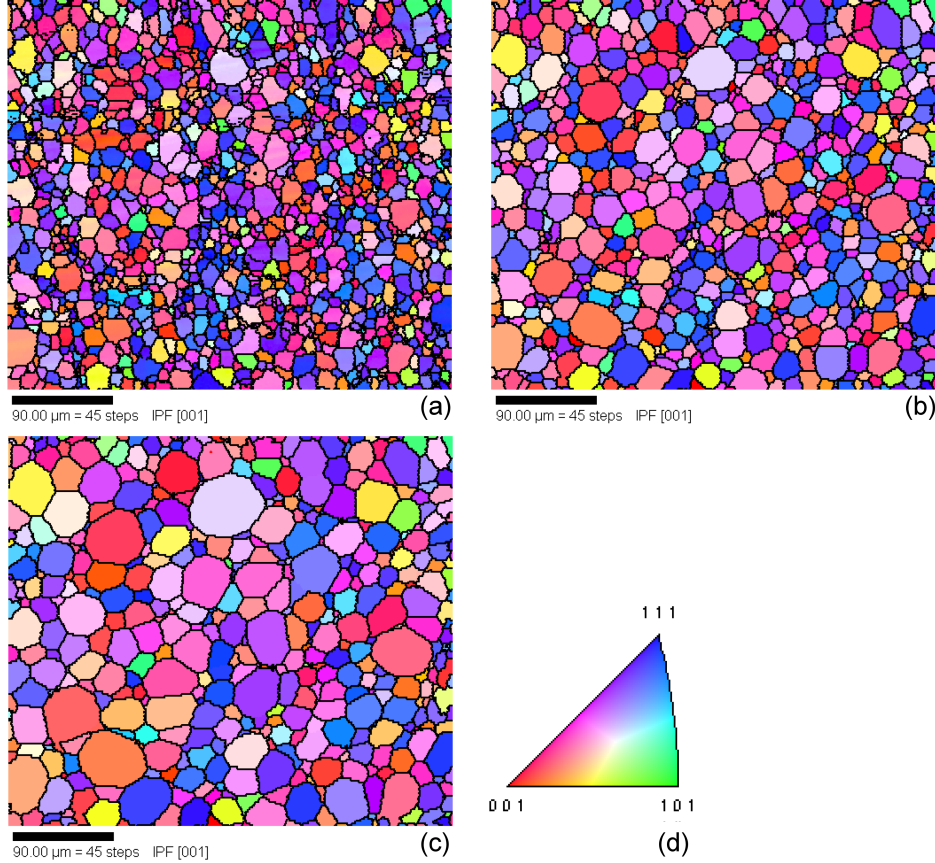


Fig. 5. Microstructural evolution after different times: $t^* = 0$ (a), $t^* = 9$ (b), and $t^* = 27$ (c). Color code defined in standard triangle (d).

of $N_0 = 1110$ grains, and its mean grain size is $\bar{R}_0 = 5.77 \mu\text{m}$. The microstructure lattice is a hexagonal grid of 200 by 203 points with a step size $\Delta = 2 \mu\text{m}$, where every lattice site is characterized by three Euler's angles $(\varphi_1, \varphi, \varphi_2)$. Two neighboring lattice points with disorientation angle $\Delta\theta \leq 2^\circ$ belong to the same grain — otherwise, a grain boundary separates the two points. In another way, the vertices and network of straights connecting them can represent the microstructure (Fig. 4b). To characterize the microstructure, one uses Orientation Imaging Microscopy (OIMTM). Figure 4c shows the initial matrix grain size distribution, which can be best fitted by the normal distribution function.

During the simulation, one uses the normalized time [18]

$$t = \frac{t^*}{m\gamma}. \quad (9)$$

To accurately describe the microstructure evolution, the step time Δt is chosen

$$\Delta t = \frac{3}{m\gamma}. \quad (10)$$

The simulation is done by MATLAB software for the isotropic cases where all energies (γ) and mobilities (m) were assumed to be uniform.

4. Results and discussion

4.1. Normal grain growth without particles

To verify that the improved vertex model properly describes the grain growth phenomenon, e.g. topological requirements and kinetics of change in mean grain size with time, one examines the kinetics for normal isotropic grain growth. The growth rate of a given grain as a function of its topology is given by von Neumann–Mullins law [29, 30]

$$\frac{dA}{dt} = \frac{\pi}{3} m\gamma (n - 6), \quad (11)$$

where A is the grain area and n is the number of its edges or neighbors.

From the mean-field approach, Hillert [31] deduced the grain size distribution in normal grain growth. Due to the poor agreement between the Hillert's distribution and the experiments, modifications to the grain size distribution have been proposed [32–35]. The basic equation that described the growth rate of the average grain size, \bar{R} , is given by [31]

$$\frac{d\bar{R}}{dt} = \frac{\alpha \bar{m} \bar{\gamma}}{4 \bar{R}} \iff \frac{d\bar{R}^2}{dt} = \frac{\alpha}{2} \bar{m} \bar{\gamma}, \quad (12)$$

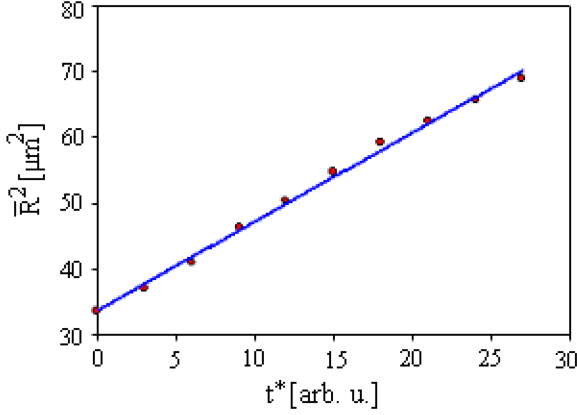


Fig. 6. Square average radius variation versus time.

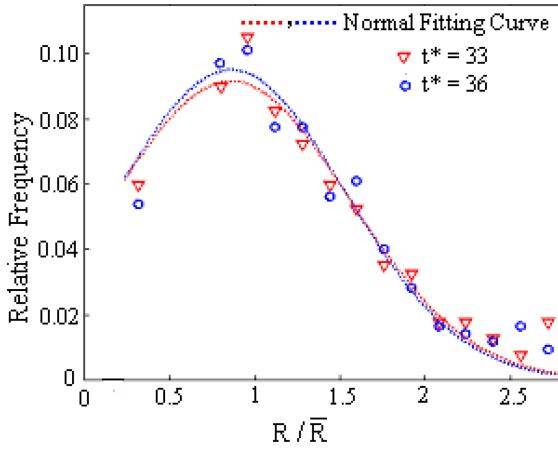


Fig. 7. Time-invariant of normalized grain size distribution.

where α is a geometrical constant that takes the value of $\frac{1}{2}$ for 2D and 1 for 3D systems, and $\bar{\gamma}$ and \bar{m} are the mean grain boundary energy and mobility, respectively.

For the case with isotropic grain boundary properties, where $\bar{\gamma}$ and \bar{m} were assumed to be uniform, (12) leads to the parabolic kinetic law

$$\bar{R}^2 - \bar{R}_0^2 = k t, \quad (13)$$

where k is the growth constant, and \bar{R}_0 is the initial average grain size at $t = 0$.

In order to test the validity of the improved model, a simulation is done for the first case for grain growth without particle consideration ($F_f = 0$). The temporal evolution of the microstructure is illustrated in Fig. 5. Colored orientation maps are used to follow the local topological and morphological evolutions of grains. After different times of simulation, normal grain growth occurs. It is clear that n -sided grains with $n > 6$ will grow, whereas grains with $n < 6$ will shrink. This behavior is in good agreement with the von Neumann–Mullins law in (11).

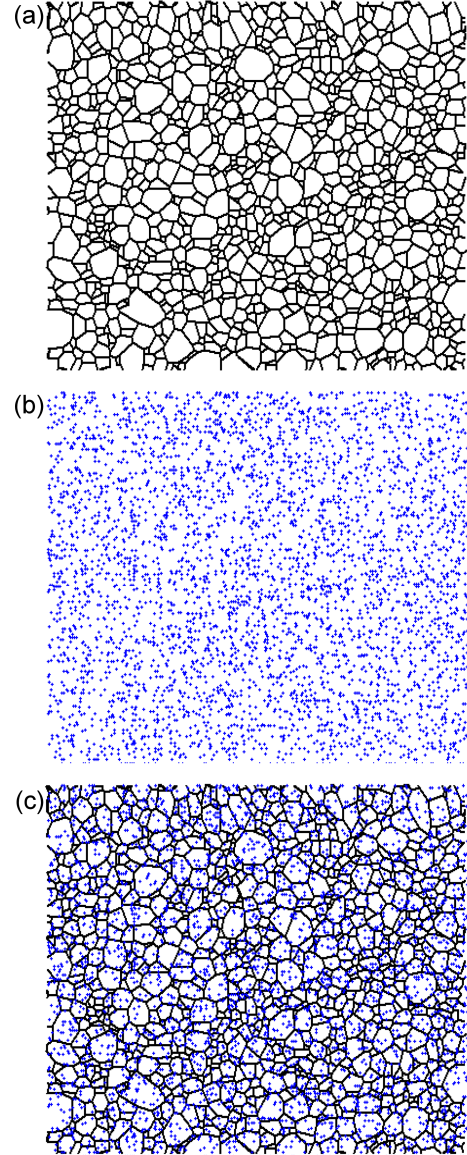


Fig. 8. (a) Grains matrix, (b) particles matrix for $f = 10\%$, and (c) combination of (a) and (b).

Figure 6 displays the change of the square mean radius as a function of time. Its dependence can be obtained by linear fitting the parabolic equation

$$\bar{R}^2 = 1.35t^* + 33.75. \quad (14)$$

In fact, (14) is in good agreement with the parabolic kinetics in (13).

With the parabolic growth kinetics, the normalized size distribution is time-invariant or self-similar, as shown for different times in Fig. 7 ($t^* = 33$ and $t^* = 36$).

4.2. Grain growth with particle pinning

During the grain growth process, immobile particles are randomly distributed between the matrix sites, i.e., on GBs and vertices. Consequently, the vertices lattice is used to locate the position of

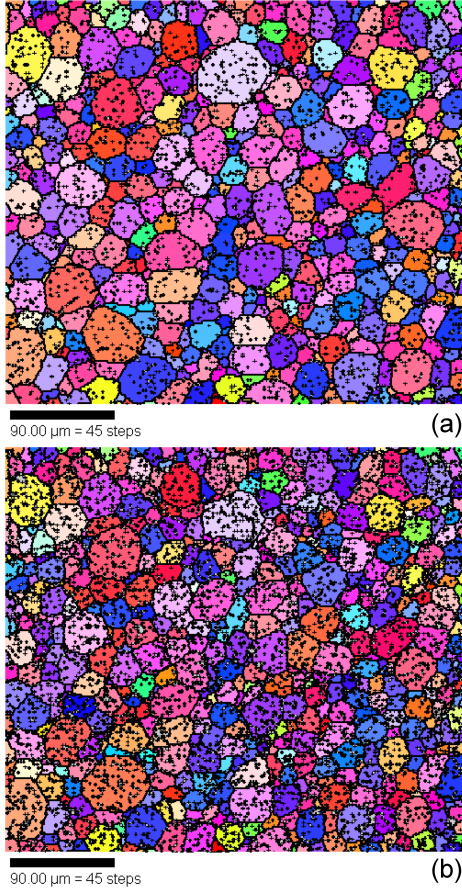


Fig. 9. Evolution of the grain structure at $t^* = 27$ for $f = 5\%$ (a) and $f = 10\%$ (b).

the particles. The present simulation is done with two input matrixes, namely the grains matrix “M” containing the experimental microstructure data (Fig. 8a) and the particles matrix “S” (Fig. 8b).

During the simulation, one uses a combination of matrices “M” and “S” as shown in Fig. 8c. So, the grains occupy only those sites of the simulated microstructure where the particles are virtually distributed without orientation.

According to Zener [3], the normal grain growth is inhibited when the matrix mean grain size \bar{R} attains the critical value

$$R_L = \frac{2}{\beta} \frac{r}{f}, \quad (15)$$

where r and f are, respectively, the average radius and the volume (surface) fraction of the particles, and β is a constant that takes the value of $\frac{4}{\pi}$ for 2D and $\frac{3}{2}$ for 3D systems.

Many modifications have been made to the Zener equation for predicting R_L in real materials. However, (15) is given in the general form

$$R_L = b \frac{r}{f^n}, \quad (16)$$

where b is a dimensionless constant and n varies between 1 and $\frac{1}{3}$ [36–39].

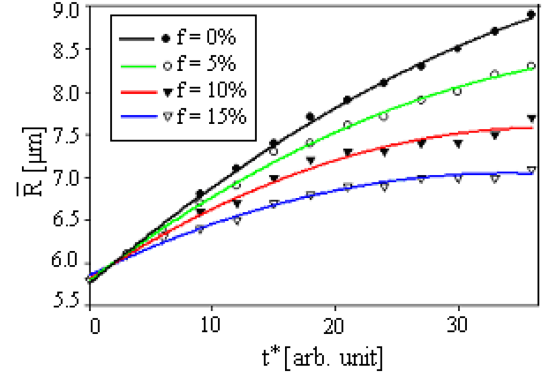


Fig. 10. Temporal development of mean grain radius for different particle fractions f .

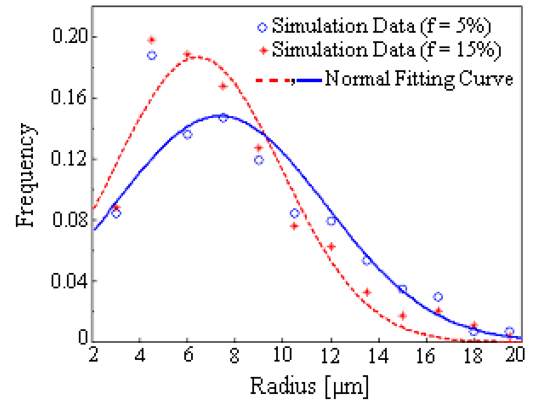


Fig. 11. Grain size distribution at $t^* = 27$ for $f = 5\%$ (blue), and $f = 15\%$ (red).

In the present work, simulations were performed for different amounts of particles: 5%, 10% and 15% area fractions. Figure 9 demonstrates the evolution of the grain structure at $t^* = 27$ for $f = 5\%$ (a) and $f = 10\%$ (b).

In Fig. 10, where each point corresponds to one simulation, the mean grain size \bar{R} for different cases is compared to the case of pure growth ($f = 0$). It is shown that growth is significantly slowed down by pinning, and nearly stopped for $f = 15\%$. Furthermore, the limiting grain size decreased as the second-phase particle fraction f increased. Comparison with experiment [40] or simulation data [13, 41] showed good agreement. Figure 11 shows a comparison of the grain size distribution at the same time $t^* = 27$, for two cases: $f = 5\%$ (a) and $f = 15\%$ (b). In the matrix containing 5% of particles there are more large grains and fewer small grains than in the matrix containing 15% particles (end and beginning of Fig. 11). This is caused by the fast growth of the grains in the matrix less pinned, i.e., in the microstructure corresponding to case (a). The size ratio of the mean radius to the initial mean radius (\bar{R}/\bar{R}_0) is equal to 1.37 and 1.20 for (a) and (b), respectively. It is clear that the grain size distribution varied with the particle concentration.

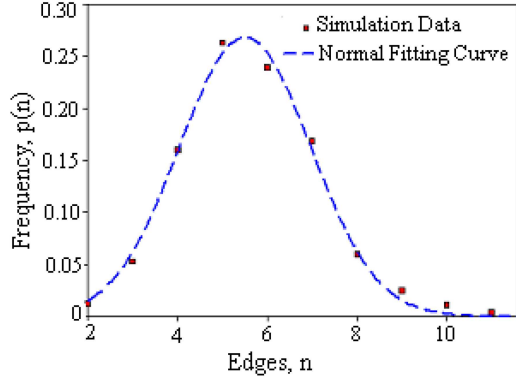


Fig. 12. Distribution of edges per grain at $t^* = 30$ for $f = 15\%$.

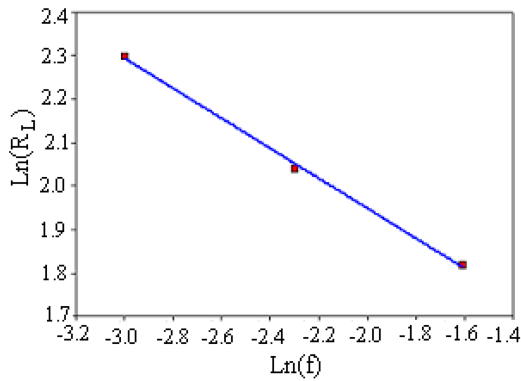


Fig. 13. Pinned mean grain size as a function of surface fraction of particles.

In two dimensions, to measure topological characteristics associated with individual grains, grains can be classified by their number of edges [42–44]. The distribution function of edges per grain, $p(n)$, is depicted in Fig. 12 at $t^* = 30$ for $f = 15\%$. It is observed that 5-sided grains have the highest frequency and 6-sided grains are the second highest, where $p(5) = 26.3\%$ and $p(6) = 23.9\%$, respectively. Our results compare well with the distribution of edges per grain as given in the following references [27, 45, 46]. The modified model has been used to predict the limiting matrix grain size R_L in the presence of particles. In the logarithmic form, (16) will be

$$\ln(R_L) = \ln(br) - n \ln(f). \quad (17)$$

Figure 13 illustrates the variation of $\ln(R_L)$ as a function of $\ln(f)$. It is well fitted by linear behavior as in (17), where $\ln(br) = 1.258 \pm 0.036$ and $n = 0.345 \pm 0.015$. The fitting value of n does not fully comply with the Zener relationship [3]. A considerable number of simulations have demonstrated that the classical Zener law cannot accurately predict the limiting mean grain size. Globally, the fitting indices n were in the range of 0.33–0.50 for 2D [13, 41, 47, 48]. For this reason, it is necessary to perform additional studies in the future.

5. Conclusions

To avoid the difficulties due to the topological changes, when using the vertex technique in the presence of second-phase particles, the simulation is done simultaneously with the matrix grid and the vertices lattice where particles are randomly distributed. The strength of the improved model is its simplicity, while no assumptions are made to the grain boundaries–particles interaction. The grain size distribution is calculated and exhibits self-similarity. The distribution of edges per grain is correctly reproduced. Different amounts of particles are used in order to study the effects of the particles surface fraction on the limiting mean grain size. Simulations have demonstrated that the classical Zener law cannot accurately predict the limiting mean grain size. Our results are in agreement with some experiments and simulation works. The present modifications improve the vertex simulation efficiency and the computational cost considerably decreases.

References

- [1] J. Humphreys, G.S. Rohrer, A. Rollett, *Recrystallization and Related Annealing Phenomena*, 3rd ed., Elsevier, Amsterdam 2017.
- [2] P.A. Beck, M.H. Holzworth, P.R. Sperry, *TMS-AIMS* **180**, 163 (1949).
- [3] C. Zener, cited by C.S. Smith, *TMS-AIMS* **15**, 175 (1948).
- [4] Y. Inokuti, C. Maeda, Y. Itoh, *Trans. ISIJ* **25**, 233 (1985).
- [5] D.J. Srolovitz, M.P. Anderson, G.S. Grest, P.S. Sahni, *Acta Metall.* **32**, 1429 (1984).
- [6] N. Maazi, R. Boulechfar, *Mater. Sci. Eng. B* **242**, 52 (2019).
- [7] D. Weygand, Y. Bréchet, J. Lépinoux, *Acta Mater.* **47**, 961 (1999).
- [8] Y. Mellbin, H. Hallberg, M. Ristinmaa, *Int. J. Sol. Struct.* **125**, 150 (2017).
- [9] Y. Li, J. Zhou, R. Li, Q. Zhang, *Front. Mater.* **8**, 682422 (2021).
- [10] S.L. Thomasa, C. Weib, J. Hana, Y. Xiangb, D.J. Srolovitz, *PNAS* **116** (18), 8756 (2019).
- [11] D. Raabe, L. Hantcherli, *Comp. Mater. Sci.* **34**, 299 (2005).
- [12] D. Wang, Y. Bai, C. Xue, Q. Wang, H. Yu, Z. Yan, *Ceram. Int.* **47**, 13669 (2021).
- [13] N. Moelans, B. Blanpain, P. Wollants, *Acta Mater.* **54**, 1175 (2006).
- [14] V. Vaithyanathan, C. Wolverton, L.Q. Chen, *Mater. Sci. Forum* **449–452**, 19 (2004).

- [15] L.Q. Chen, *Scr. Metall. Mater.* **32**, 115 (1995).
- [16] J. Roessiger, P. D. Bons, A. Griera, M.W. Jessell, L. Evans, M. Montagnat, S. Kipfstuhl, S.H. Faria, I. Weikusat, *J. of Glaciology* **57**, 942 (2011).
- [17] A.G. Fletcher, J.M. Osborne, P.K. Maini, D.J. Gavaghan, *Prog. Biophys. Mol. Bio.* **113**, 299 (2013).
- [18] N. Maazi, *Acta Phys. Pol. A* **141**, 467 (2022).
- [19] T.F.W. van Nuland, L.P. Belotti, J.A.W. van Dommelen, M.G.D. Geers, *Modell. Simul. Mater. Sci. Eng.* **29**, 085014 (2021).
- [20] K. Piekos, J. Tarasiuk, K. Wierzbowski, B. Bacroix, *Comput. Mater. Sci.* **42**, 584 (2008).
- [21] K. Kawasaki, T. Nagai, K. Nakashima, *Phil. Mag. B* **60**, 399 (1989).
- [22] A. Soares, A.C. Ferro, M.A. Fortes, *Scr. Metall.* **19**, 1491 (1985).
- [23] T. Tamaki, K. Murakami, K. Ushioda, *ISIJ Int.* **56** (10), 1857 (2016).
- [24] G. Gottstein, L.S. Shvindlerman, *Scr. Mater.* **54**, 1065 (2006).
- [25] P. Streitenberger, D. Zöllner, *Acta Mater.* **78**, 114 (2014).
- [26] P.R. Rios, M.E. Glicksman, *Phil. Mag.* **95**, 2092 (2015).
- [27] C.E. Torres, M. Emelianenko, D. Golovaty, D. Kinderlehrer, S. Taasan, *SIAM J. Appl. Math.* **75** (2), 762 (2015).
- [28] N. Moelans, B. Blanpain, P. Wollants, *Acta Mater.* **55**, 2173 (2007).
- [29] J. von Neumann, *J. Met. Interfaces* **1952**, 108 (1952).
- [30] W.W. Mullins, *J. Appl. Phys.* **27**, 900 (1956).
- [31] M. Hillert, *Acta Metall.* **13**, 227 (1965).
- [32] C.S. Pande, *Acta Metall.* **35**, 2671 (1987).
- [33] P.R. Rios, T.G. Dalpian, V.S. Brandao, J.A. Castro, A.C.L. Oliveira, *Scr. Mater.* **54**, 1633 (2006).
- [34] A. Gadomski, N. Kruszewska, *Eur. Phys. J. B* **85**, 416 (2012).
- [35] T. Breithaupt, L.N. Hansen, S. Toppaladoddi, R.F. Katz, *Acta Mater.* **209**, 116699 (2021).
- [36] H.C. Ming, C.L. Joanne, B.S.V. Patnaik, R. Jayaganthan, *Appl. Surf. Sci.* **252**, 3997 (2006).
- [37] K.R. Phaneesh, A. Bhat, P. Mukherjee, K.T. Kashyap, *Comput. Mater. Sci.* **58**, 188 (2012).
- [38] M. Hillert, *Acta Metall.* **36**, 3177 (1988).
- [39] C.L.D. Prinzio, E. Druetta, O.B. Nasello, *Modell. Simul. Mater. Sci. Eng.* **21**, 025007 (2013).
- [40] J.D. Hutchinson, F.A. Lavergne, R.P.A. Dullens, *Phys. Rev. Mater.* **6**, 075604 (2022).
- [41] Y. Wu, J. Xiong, Q. Luo, J. Chen, R. Zeng, S. Wang, *Crystals* **12**, 1504 (2022).
- [42] V. Fradkov, D. Udler, *Adv. Phys.* **43**, 739 (1994).
- [43] W. Fayad, C.V. Thompson, H.J. Frost, *Scr. Mater.* **40**, 1199 (1999).
- [44] L. Meng, H. Wang, G. Liu, Y. Chen, *Comput. Mater. Sci.* **103**, 165 (2015).
- [45] D. Fan, C. Geng, L.Q. Chen, *Acta Mater.* **45**, 1115 (1997).
- [46] G.M. La Boissonière, R. Choksi, K. Bar-mak, S. Esedoglu, *Materialia* **6**, 100280 (2019).
- [47] J.J. Li, J.C. Wang, G.C. Yang, *Rare Met. Mater. Eng.* **10**, 1746 (2008).
- [48] L. Du, S. Yang, P. Zhang, H. Du, *Compos. Inter.* **25**, 357 (2018).